Plasmon Enhancement Mechanism for the Upconversion Processes in $NaYF_4:Yb^{3+},Er^{3+}$ Nanoparticles: Maxwell *versus* Förster

[Dawei Lu†](), [Suehyun K. Cho†](), [Sungmo Ahn†](), [Loic Brun§](), [Christopher J. Summers§](), and [Wounjhang Park†‡*]()

†Department of Electrical, Computer & Energy Engineering and ‡Materials Science & Engineering Program, University of Colorado, Boulder, Colorado 80309, United States

§ School of Materials Science & Engineering, Georgia Institute of Technology, Atlanta, Georgia 30332, United States

ACS Nano, **2014**, *8* (8), pp 7780–7792

DOI: 10.1021/nn5011254

*Address correspondence to won.park@colorado.edu.

Abstract

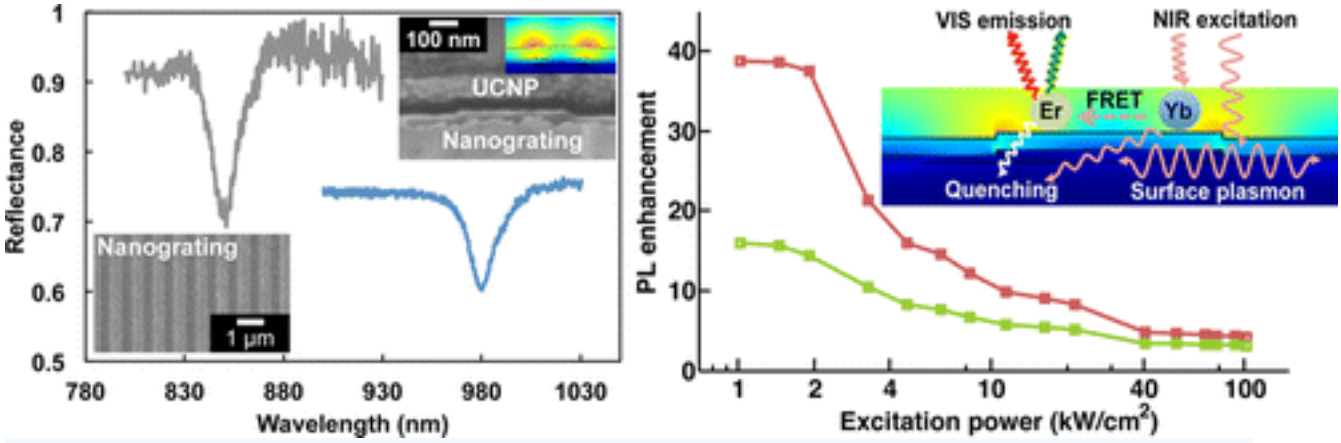

Rare-earth activated upconversion materials are receiving renewed attention for their potential applications in bioimaging and solar energy conversion. To enhance the upconversion efficiency, surface plasmon has been employed but the reported enhancements vary widely and the exact enhancement mechanisms are not clearly understood. In this study, we synthesized upconversion nanoparticles (UCNPs) coated with amphiphilic polymer which makes UCNPs water soluble and negatively charged. We then designed and fabricated a silver nanograting on which three monolayers of UCNPs were deposited by polyelectrolyte-mediated layer-by-layer deposition technique. The final structures exhibited surface plasmon resonance at the absorption wavelength of UCNP. The green and red photoluminescence intensity of UCNPs on nanograting was up to 16 and 39 times higher than the reference sample deposited on flat silver film, respectively. A thorough analysis of rate equations showed that the enhancement was due entirely to absorption enhancement in the strong excitation regime, while the enhancement of both absorption and Förster

energy transfer contribute in the weak excitation regime. The Purcell factor was found to be small and unimportant because the fast nonradiative decay dominates the relaxation process. From the experimentally observed enhancements, we concluded 3.1× and 1.7× enhancements for absorption and Förster energy transfer, respectively. This study clearly shows the plasmon enhancement mechanism and its excitation power dependence. It provides the basis for comparison of the enhancements of various plasmonic UCNP systems in the literature. It also lays the foundation for rational design of optical plasmonic structures for upconversion enhancement.

Keywords:
absorption enhancement; Förster energy transfer; photoluminescence; Purcell effect; surface plasmon; upconversion

Frequency conversion has long been a topic of great interest in optics. Since the demonstration of second-harmonic generation over a half-century ago,(1, 2) nonlinear optics demonstrating a variety of frequency conversion mechanisms has become one of the greatest success stories in science, spawning a wide range of applications in information, medical, industrial, and military technologies. Typically, frequency conversion is based on the nonlinear susceptibility that results in intensity-dependent nonlinear refractive index and consequently enables a variety of frequency conversion mechanisms such as high harmonic generation, parametric oscillation, and four-wave mixing. While highly successful, the frequency conversion by nonlinear susceptibility has a fundamental limitation in that it requires a high-intensity, coherent light source. In contrast, frequency conversion by optically active ions is known to be far more efficient than high harmonic generation or two-photon absorption.(3, 4) It does not require phase matching and can be accomplished with incoherent light sources. Thus, frequency-converting phosphors activated with rare earth or transition metal ions are ideally suited for applications in lighting, solar energy conversion and biomedical imaging. In particular, interest in upconversion phosphors have been renewed in recent years due to their potential for significantly enhancing the efficiencies of photovoltaic devices.(5, 6) There exist many different types of upconversion phosphors exhibiting frequency upconversion by energy transfer upconversion (ETU), excited-state absorption, cooperative sensitization, and cooperative luminescence.(1, 2, 7) Among them, the most efficient mechanism is ETU where two sensitizer ions transfer energy to a single activator ion successively to achieve frequency upconversion. The most efficient material is known to be $NaYF_4$:Yb^{3+},$Er^{3+}$with energy conversion efficiencies up to 4% at pump intensities around 10 W/cm^2.(3, 4, 8)

For widespread applications, the efficiency needs to be improved further, and plasmonics offer a promising avenue for this. Storing a fraction of its energy in electron gas, surface plasmons are

highly effective in creating a strongly localized and intense optical field which consequently enhances a variety of optical processes. The best-known example is surface-enhanced Raman scattering (SERS). Using a rough silver surface, Raman scattering by a single molecule has been observed with enhancements up to a factor of 10^{14}.(5, 6, 9, 10) Much of the enhancement is believed to arise from the local field enhancement due to the hot spots produced by the silver nanostructure. (7, 11) Surface plasmon resonance can also be used to enhance luminescence(8, 12-21) and Förster energy-transfer process.(9, 10, 14, 16) For luminescence upconversion, a recent theoretical study showed the enhancement of upconverted luminescence has a fourth power dependence on the local field enhancement, $|E_{loc}/E_0|^4$, in contrast to the square dependence, $|E_{loc}/E_0|^2$, of luminescence enhancement.(11, 22) While the quenching issue still has to be dealt with, this raises the hope for dramatic enhancement in upconversion efficiency by the local field enhancement effect. Naturally, there has been a plethora of reports on plasmonic enhancement of upconverted luminescence.(12-21, 23) However, as commonly experienced with newly emerging topics, there appears to be a great deal of confusion on what exactly the enhancement mechanism is and how much enhancement is achievable. For example, the reported enhancement factors in upconverted luminescence intensity vary widely between 3 and 310.(14, 16, 24) There are many reasons for the discrepancies. Obviously, various geometries exhibiting different local field enhancement would lead to different enhancement factors. However, the upconversion efficiency itself is a function of excitation power, and thus, the enhancement factors from the same sample could vary widely depending on the experimental conditions, which are not always clearly described. Furthermore, ETU is a complex process involving multiple steps with distinct physical processes. Specifically, the enhanced local field can influence light absorption, emission, and Förster energy transfer. Therefore, enhanced upconverted luminescence does not always mean enhancement of the Förster energy-transfer process as often claimed, and the enhancements of all involved processes must be carefully analyzed to properly understand their contributions and interplay between them. In this paper, we present our experimental results on the plasmon enhancement of upconverted luminescence in $NaYF_4:Yb^{3+},Er^{3+}$ nanoparticles together with a thorough analysis based on the rate equations describing the ETU process. Our study shows the enhancement factor is highly sensitive to the excitation condition. We determine separately the enhancements in absorption, emission (Purcell effect), and Förster energy transfer and show which contributions are important under different excitation conditions. As will be shown later, absorption enhancement plays the dominant role in general, the enhancement of Förster energy transfer is important only under weak excitation conditions, and the Purcell effect is unimportant.

•

Results

The $NaYF_4$:Yb^{3+},Er^{3+} upconversion nanoparticles (UCNP) were synthesized by the coprecipitation method.(22, 25) As shown in the transmission electron micrographs (TEM) in Figure 1a, the nanoparticles were regular hexagonal platelets, indicating the formation of β-phase $NaYF_4$nanocrystals. The mean lateral size was 32 nm. The Yb^{3+} and Er^{3+} doping densities were 18% and 2%, respectively. The UCNPs were of good optical quality and exhibited strong upconverted luminescence under the excitation at 980 nm. The as-synthesized UCNPs are covered with oleic acid and thus not water-soluble. To make them water-soluble and also to make the nanoparticle surface negatively charged, we coated the nanoparticles with poly(maleic anhydride-*alt*-1-octadecene) (PMAO). The Inset of Figure 1a shows a thin and uniform coating of PMAO on UCNPs. The mean coating thickness was 2 nm. The PMAO-coated UCNPs can then be deposited uniformly in a layer-by-layer (LBL) fashion with precisely controlled thickness, as described in the Methods. To study the plasmon enhancement effect, a one-dimensional (1D) silver nanograting was fabricated on a 200 nm thick silver film by the nanoimprint lithography (NIL). Since the fabrication process involved oxygen plasma treatment as described in the Methods, a 10 nm thick gold layer was first deposited on the 200 nm thick silver film in order to prevent oxidation of silver. The subsequent nanopatterning by NIL and lift-off resulted in 20 nm thick and 410 nm wide silver lines with a period of 830 nm, as shown in the scanning electron micrograph (SEM) in Figure 1b. On the silver nanograting, a 30 nm thick Si_3N_4 spacer layer was first deposited by the chemical vapor deposition to alleviate luminescence quenching by the metal surface, and then three monolayers of UCNPs were deposited by the LBL method using poly(allylamine hydrochloride). The thickness of the LBL UCNP layers was measured by atomic force microscopy, and the three monolayers of UCNPs were found to be 90 nm thick (Supporting Information). The nanograting parameters were chosen by the finite element modeling so that the structure should support surface plasmon mode at 980 nm after the deposition of the Si_3N_4 spacer layer and three monolayers of UNCPs. For comparison's sake, reference samples were also prepared by depositing a 30 nm thick Si_3N_4 and three monolayers of UCNPs on the flat silver surfaces with 10 nm thick gold film on top. The metal surface can affect luminescence in three different ways: plasmon enhancement, quenching, and reflection of excitation laser beam and backward-emitted luminescence. The flat metal surface was chosen as reference because it presents the same degree of quenching and reflection as the nanograting surface. The difference between the reference and nanograting samples should therefore be solely due to the plasmon effect.

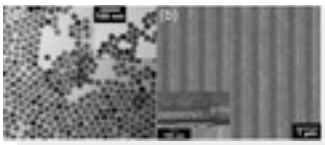

Figure 1. (a) TEM of as-synthesized β-phase $NaYF_4$:Yb^{3+},Er^{3+} UCNPs. The mean lateral size was 32 nm. The inset shows the TEM of PMAO-coated UCNPs showing a uniform 2 nm thick coating. The scale bar applies to both TEM images. (b) SEM of silver nanograting with period of 830 nm and line width of 410 nm. The inset shows the cross-sectional SEM of grating-Si_3N_4-UCNPs. The black layer in the middle is 30 nm Si_3N_4 coating sitting on top of the nanograting. Above the Si_3N_4 layer are the three monolayers of UCNPs. The thickness was consistent with the atomic force microscopy measurements. To acquire good quality images, a thick gold overlayer was deposited on top of UCNPs for this sample.

The fabricated samples were characterized by reflectance and photoluminescence (PL) spectroscopy. The reflectance spectra were taken at normal incidence, and the samples did not have any transmission due to the thick silver substrate. As shown in Figure 2a, the as-fabricated silver nanograting exhibited a well-defined dip at 850 nm due to the coupling to the surface plasmon mode. Upon deposit of the Si_3N_4 spacer layer and three layers of UCNPs, the plasmon peak shifted to 980 nm, as designed. The red shift is due to the increased effective index of the dielectric half-space and is consistent with the theory for surface plasmon modes on the dielectric-loaded metal surface.(23, 26-31) The background reflectance was reduced to around 0.75 after UCNP deposition, indicating some light scattering due to the roughness of the UCNP surface. However, the UCNP film was uniform enough to preserve a strong and well-defined dip due to the surface plasmon resonance. To further confirm the existence of surface plasmon mode and to estimate the anticipated field enhancement effect, we performed the finite element modeling using the structural parameters as measured by SEM shown in Figure 1b. The gold and silver dielectric functions were based on the experimentally measured bulk values,(24, 32, 33) except that the imaginary part was increased to account for the increased loss due to electron scattering by the grain boundaries.(25, 31) As shown in Figure 2a, an excellent agreement was found between experimental and simulated reflectance spectra, indicating the high optical quality of the samples used in this study. Once the presence of surface plasmon mode was confirmed experimentally, we conducted PL spectroscopy using 980 nm laser excitation. As shown in Figure 2b, both the UCNPs on nanograting and the reference sample on flat silver surface exhibited green and red emission bands, which were attributed to the $^4S_{3/2}$, $^2H_{11/2} \rightarrow {}^4I_{15/2}$, and $^4F_{9/2} \rightarrow {}^4I_{15/2}$ transitions of Er^{3+} ion (Figure 3), respectively. However, the UCNPs on nanograting showed much stronger PL intensities under all excitation power densities. Figure 2b shows the PL spectra taken under the excitation power density of 1 kW/cm^2, which exhibited 16× and 39× enhancements in the green and red PL peak intensities,

respectively. The enhanced PL intensities in the UCNPs on nanograting are direct evidence of the local field enhancement effect due to surface plasmon. For completeness, we have also measured upconverted luminescence from the UCNPs deposited on a glass substrate. The UCNPs on nanograting exhibited up to 25× and 31× enhancement in green and red emission, respectively, demonstrating that the UCNPs on nanograting show overall enhancement of upconversion efficiency over both metallic and nonmetallic surfaces.

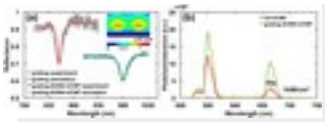

Figure 2. (a) Experimental reflectance spectra of as-fabricated nanograting (gray) and nanograting-Si_3N_4-UCNP structure (blue). The simulated reflectance spectra for the two structures are also plotted with red and green lines. The inset shows the field profile at the resonance wavelength for the nanograting-Si_3N_4-UCNP sample under normally incident plane wave excitation with a power density of 1.2 MW/m^2. (b) PL spectra of reference sample on flat metal film (red) and nanograting-Si_3N_4-UCNP sample (green). The excitation wavelength and power density were 980 nm and 1 kW/cm^2, respectively. PL intensity of reference UCNP sample is magnified by 10-fold for better visualization.

The ETU mechanism for luminescence upconversion in Yb^{3+},Er^{3+} coactivated materials has been studied previously.(26-31) The major processes are shown schematically in Figure 3. Most of the incident light is absorbed by the Yb^{3+} ions because they have nine times higher doping density in our samples and exhibit a much larger absorption cross-section than the Er^{3+} ions.(32-34) The absorption of the incident photon thus excites the Yb^{3+} ion into the $^2F_{5/2}$ level, from which the Yb^{3+} ion decays back to the ground level, $^2F_{7/2}$, *via* the Förster energy-transfer process, exciting a nearby Er^{3+} ion into the $^4I_{11/2}$ level. If the energy transfer takes place one more time before the excited Er^{3+} ion decays back to the ground state, the Er^{3+} ion is excited to the $^4F_{7/2}$ level and then quickly decays nonradiatively to the $^2H_{11/2}$ and $^4S_{3/2}$ levels from which the green luminescence occurs. A fraction of Er^{3+} ions in the $^4S_{3/2}$ state would decay nonradiatively into the slightly lower $^4F_{9/2}$ level where the red luminescence originates. An additional path for the red emission is for the Er^{3+} ion in $^4I_{11/2}$ level to decay nonradiatively into the $^4I_{13/2}$ level and then get excited to the $^4F_{9/2}$ level by the Förster energy transfer from a nearby Yb^{3+} ion. There are other processes that compete with the ETU process such as radiative and nonradiative decays from $^2F_{5/2}$ of Yb^{3+} and $^4I_{11/2}$ of Er^{3+}, back energy transfer from Er^{3+} to Yb^{3+}, and cross-relaxation of Er^{3+} ion pairs. The cross relaxation of Er^{3+} ions offers a major quenching mechanism at high Er^{3+} concentrations.(31, 34) Furthermore, there are three-photon upconversion processes, resulting in blue emission and also contributing to the green and red emission.(30, 34) However, it is expected and has been experimentally demonstrated, as shown

later, that the three-photon processes make much smaller contributions than the two-photon processes and are therefore omitted in our analysis of green and red luminescence intensities.

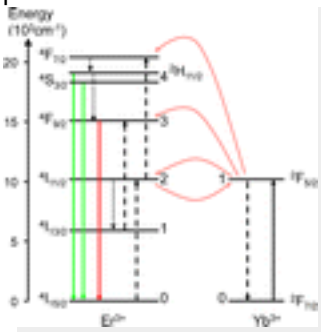

Figure 3. Energy levels of Yb^{3+} and Er^{3+} ions relevant to the energy-transfer upconversion process. Initial absorption is indicated by the black solid line arrow, subsequent energy transfer processes by the dashed arrows, nonradiative relaxations by dotted arrows, and the final upconverted luminescence by the green and red arrows.

Upconverted luminescence is known to exhibit distinct power-law dependence on the excitation power density.(34, 35) In the weak excitation limit, the upconverted luminescence intensity is proportional to the k^{th} power of the excitation power density where k is the number of upconversion steps involved. In the strong excitation limit, however, the upconverted luminescence intensity is simply proportional to the excitation power density. The distinction between the weak and strong excitation conditions is made by comparing the rates of upconversion and decay. For a given energy level in the upconverting system, we anticipate two competing processes: upconversion to a higher energy level and decay (radiative and nonradiative) into a lower energy level. In the weak excitation limit, decay process is dominant, while in the strong excitation limit, upconversion process dominates. This approximation greatly simplifies the rate equations and leads to the distinct power dependence described above, which has also been verified experimentally.(34, 36)

To investigate the plasmonic effect on the excitation power dependence, we measured the visible emission intensity under various excitation power densities. Figure 4 shows the power dependence of the green and red emission intensities for UCNPs on silver nanograting and on flat silver film (reference sample). For both green and red emission, the luminescence intensity exhibited quadratic and linear dependence on the excitation power density at low and high power densities, respectively. This is consistent with the previous report by Suyver *et al.*(34, 35, 37-42)and indicates the upconversion processes for both green and red emission are dominated by two-step ETU with negligible contributions by three-step processes. The power dependence of UCNPs on silver nanograting was identical to that of the reference sample for both green and red emission, except that the transition between weak and strong excitation regimes occurred at lower power densities.

This result clearly shows that the plasmon resonance increases the local optical power density. From Figure 4a,b, the power densities at which the transition between weak and strong excitation regimes occurs were estimated to be 3.6 and 5.0 times lower for the green and red emission from the nanograting sample compared to the reference sample. These numbers provide an estimate of how much local optical power density is enhanced in the plasmonic grating sample and agree well with the absorption enhancement factor derived later.

The observed shift in the power dependence consequently results in a power-dependent enhancement factor, which is defined as the ratio of integrated emission intensity between UCNPs on nanograting and reference samples. It should be noted that we calculated the emission pattern for the nanograting and reference samples as described in Methods and found the difference to be negligibly small. The observed photoluminescence enhancement is therefore the actual enhanced UCNP emission. As shown in Figure 4c, the enhancement factor for green emission varied from 3.1 to 16.0 while the red emission enhancement factor changed from 4.2 to 38.8. We note that the enhancement factor is independent of excitation power in the low and high power limits while it changes rapidly in the intermediate region. Therefore, when discussing the plasmon enhancement effects in upconversion materials, it is imperative to specify the excitation power density and identify whether the measurements were taken in the weak, intermediate, or strong excitation regimes. The inherent power dependence of enhancement factor explains in part the wide variations in the reported values of enhancement factors found in the literature.

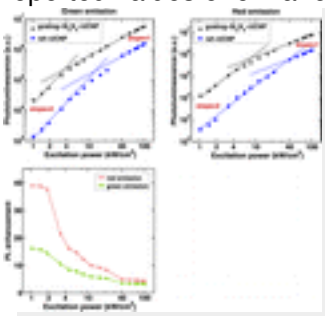

Figure 4. (a) Green and (b) red photoluminescence intensities under various excitation power densities. The UCNPs on silver nanograting is denoted with black open circles, while the reference sample on flat metal film is represented by blue filled circles. The blue and black dash lines are obtained by the least-squares fitting with the slopes of 1 and 2 as denoted. (c) Enhancement factors of the green (green filled circles and line) and red (red open circles and line) upconverted luminescence as a function of the excitation power density.

Discussion

For complete understanding of the plasmon enhancement mechanism, we set up rate equations describing all key processes affecting the ETU mechanism. In our rate equations, the $^4F_{7/2}$ level of Er^{3+} is not included as the relaxation from the $^4F_{7/2}$ level to the lower lying $^2H_{11/2}$ and $^4S_{3/2}$ levels is known to be extremely fast.(26, 29, 35, 42-44) Also, the $^2H_{11/2}$ and $^4S_{3/2}$ levels are close enough to be considered as a single level. The complete set of rate equations is then written as

$$\frac{dN_{D1}}{dt} = \sigma\Phi N_{D0} - W_{D10}N_{D1} + c_{Bd2}N_{A2}N_{D0} - c_{Fd2}N_{D1}N_{A0} - c_{d3}N_{D1}N_{A1} - c_{d4}N_{D1}N_{A2} \quad (1)$$

$$\frac{dN_{A1}}{dt} = W_{A21}N_{A2} - W_{A10}N_{A1} - c_{d3}N_{D1}N_{A1} \quad (2)$$

$$\frac{dN_{A2}}{dt} = c_{Fd2}N_{D1}N_{A0} - c_{Bd2}N_{A2}N_{D0} - c_{d4}N_{D1}N_{A2} - W_{A20}N_{A2} - W_{A21}N_{A2} \quad (3)$$

$$\frac{dN_{A3}}{dt} = W_{A43}N_{A4} + c_{d3}N_{A1}N_{D1} - W_{A30}N_{A3} \quad (4)$$

$$\frac{dN_{A4}}{dt} = C_{d4}N_{D1}N_{A2} - W_{A40}N_{A4} - W_{A43}N_{A4} \quad (5)$$

$$N_D = N_{D0} + N_{D1} \quad (6)$$

$$N_A = N_{A0} + N_{A1} + N_{A2} + N_{A3} + N_{A4} \quad (7)$$

Here N_i is the density of ions in the energy level i. The subscripts D1 and D0 represent the $^2F_{5/2}$and $^2F_{7/2}$ levels of donor (Yb^{3+}), respectively, and A4, A3, A2, A1, and A0 indicate the $^4S_{3/2}$, $^4F_{9/2}$, $^4I_{11/2}$, $^4I_{13/2}$, and $^4I_{15/2}$ levels of acceptor (Er^{3+}), respectively. W is the decay rate, and the subscript indicates the initial and final states of the transition. For example, W_{D10} is the decay rate of donor ion from D1 to D0 state. c_{d2}, c_{d3}, and c_{d4} are the energy-transfer coefficients for the Förster energy transfer processes between the donor and the acceptor in the A2, A3, and A4 levels, respectively. The additional subscripts F and B in the c_{d2} coefficient indicate the forward (donor to acceptor) and backward (acceptor to donor) energy transfers. Finally, N_D and N_A are the doping densities of donor and acceptor, respectively, σ is the absorption cross section of the donor ion, and Φ is the incident light flux. It is noted that the three-photon ETU processes are not included in the rate equations as they should in general have much lower probability than the two-photon mechanism.(4, 11, 36) Also omitted for simplicity are the transitions from the $^4S_{3/2}$ level to the

intermediate energy levels, $^4I_{11/2}$ and $^4I_{13/2}$, which are generally weak, although they may become significant when the $^4S_{3/2}$ population is high. Furthermore, we consider only the backward transfer from the acceptor $^4I_{11/2}$ level to donor as the lifetimes of the higher excited states of the acceptor are so short that back-transfer is negligible. Finally, the decay rate, *W*, should in general include the rate of both radiative and nonradiative decays. In conventional $NaYF_4$:Yb^{3+},Er^{3+}samples, the major nonradiative decay channel is multiphonon emission, but thanks to the small phonon energy of the fluoride host, the nonradiative decay rate is usually small. Thus, *W* is typically replaced with the radiative decay rate. In our case, however, the UCNPs are in close proximity of the metal surface and the energy transfer to metal offers a highly efficient nonradiative decay channel, and therefore, nonradiative decay rate should not only be included but could very well dominate. This was confirmed by the time-resolved photoluminescence spectroscopy. UCNPs exhibit infrared luminescence due to the direct radiative decay from $^2F_{5/2}$ to $^2F_{7/2}$ and also from the $^4I_{11/2}$ to $^4I_{15/2}$ levels. Since these emission bands are too close to our excitation laser, we could not fully resolve the entire emission band. In fact, even after strong attenuation by a sharp-edged long-pass filter, a strong laser peak was persistent. Nevertheless, we were able to observe the long wavelength tails of the UCNP emission. As shown in Figure 5(a), the emission band peaking at 1005 nm was observed only from the UCNP containing samples but not from the scattered laser light, confirming this emission band originates from the UCNPs. Then, the luminescence decay was monitored at 1005 nm followed by a pulsed excitation. We used a train of square pulses with a pulse width of 23 ms and a period of 42 ms. Both the pulse width and the interval between two successive pulses were chosen to be much longer than the rise and decay times of the upconverted luminescence so that the system reaches steady state before the excitation pulses are turned on and off. As shown in Figure 5b, the UCNPs deposited on glass exhibited an exponential decay with a lifetime of 1.7 ms. This value is consistent with the radiative decay time previously reported in the literature(35, 37-42, 45-48) and is indicative of small nonradiative decay and high material quality. The UCNPs on nanograting and flat silver film both showed much faster decay with lifetimes of 201 and 199 μs, respectively. As shown later, the Purcell factor is close to unity. Thus, the large reduction in decay time is due to the luminescence quenching by metal, which appears to persist despite the use of the 30 nm Si_3N_4 spacer layer. An important point, however, is that both the UCNPs on nanograting and flat silver film exhibited the same decay time. Thus, W_{A20} and W_{D10}, dominated by nonradiative energy transfer to metal, remain the same in both the nanograting and the reference samples.

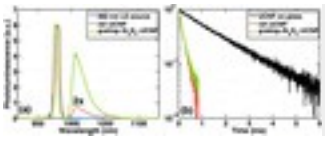

Figure 5. (a) Photoluminescence spectra of a 980 nm laser diode source (blue, magnified 2×), reference sample on flat metal film (red, magnified 2×), and nanograting sample (green). The UCNP emission profile is modulated by a 997 nm long pass edge filter, which attenuates the scattered laser light. (b) Photoluminescence decay at 1005 nm for the UCNPs on glass (black), reference sample (red), and nanograting sample (green) under 1.9 kW/cm^2 excitation power density.

Since the rate equations given above are rather unwieldy, even after the omission of three-photon processes, it is profitable to seek for further simplifying approximations. Many groups have ignored the red emission entirely.(26, 29, 33, 35, 37, 42-44, 49) Others assumed fast equilibrium between the $^2F_{5/2}$ level of Yb^{3+} and the $^4I_{11/2}$ level of Er^{3+},(4, 11, 44, 49, 50) and yet other groups ignored the back energy transfer from Er^{3+} to Yb^{3+}.(39, 42, 45-48, 51) However, the justifications for these approximations are often dubious. As shown in Figures 2 and 4, red emission is clearly not negligible and is dominant at high excitation power densities. The assumption of fast equilibrium requires the c_{Fd2} and c_{Bd2} coefficients are so large that the forward and backward energy transfer rates are much greater than the radiative and nonradiative decay rates. Ignoring backward energy transfer means $c_{Fd2} \gg c_{Bd2}$, which is at odds with the assumption of fast equilibrium. The problem lies in the difficulty in directly measuring the energy transfer coefficients. There is naturally a dearth of data on energy transfer coefficients. However, the few that reported the values of energy transfer coefficients indicate that c_{Fd2} and c_{Bd2} are of the same order of magnitude(33, 37, 43, 44, 49, 51, 52) and the energy transfer rates may be comparable to the decay rates.(44, 49-55)Although the values of energy transfer coefficients depend strongly on the doping densities and the host material, the approximations mentioned above appear to be poorly justified and we therefore proceed with the full set of eqs 1–7 to investigate the behaviors in the weak and strong excitation limits. The details on how to obtain steady-state solutions of the rate equations under continuous-wave excitation are given in the Supporting Information. The essence of the approximations made for weak and strong excitation limits is to consider the competition between the upconversion processes and decay processes for the intermediate energy levels, $^2F_{5/2}$ and $^4I_{11/2}$. In the weak excitation regime, decay processes dominate while the upconversion processes become dominant in the strong excitation regime. These approximations allow significant simplifications and offer simple and revealing solutions. In the weak excitation limit, the green and red photon emission rates (in units of per

$$\Phi_G = \frac{W_{A40}}{W_{A4}} \frac{c_{d4} c_{Fd2} N_A N_D}{c_{Bd2} W_{D10}^2} (\sigma\Phi)^2 \qquad (8)$$

volume per time) are given as

$$\Phi_R = \left(\frac{W_{A43} c_{d4}}{W_{A4}} + \frac{W_{A21} c_{d3}}{W_{A10}} \right) \frac{c_{Fd2} N_A N_D}{c_{Bd2} W_{D10}^2} (\sigma\Phi)^2 \qquad (9)$$

Here, the W_{A4} is the total decay rate of energy level A4, $W_{A4} = W_{A40} + W_{A43}$. Equations 8 and 9clearly show the quadratic dependence on the incident photon flux, which is a consequence of the two-photon process responsible for upconversion and is also consistent with the experimental data in Figure 4. In addition, they show the upconverted luminescence intensity should increase linearly with the donor and acceptor densities. Also, the upconverted luminescence intensity varies linearly with the energy transfer coefficients, c_{Fd2} and c_{d4}, and inversely with c_{Bd2} and the square of donor decay rate, W_{D10}. In the strong excitation limit, the green and red photon emission rates are found to

$$\Phi_G = \frac{W_{A40}}{W_{A4}} \frac{N_{D0}}{2} \sigma\Phi \qquad (10) \qquad \Phi_R = \frac{W_{A43}}{W_{A4}} \frac{N_{D0}}{2} \sigma\Phi \qquad (11)$$

be

Equations 10 and 11 show the linear power dependence on the excitation power density as observed in Figure 4. Also, it is important to note that the upconverted luminescence intensity depends only on the donor density and excitation power density but not on any of the energy transfer coefficients since, in the strong excitation limit, the energy transfer rate is so fast that the upconversion is limited by the absorption by the donor ion.

The simplified expressions in eqs 8–11 provide the basis for determining the plasmon enhancement effects on the various processes involved in upconversion. The enhancement factors, F_{weak} and F_{strong}, for the green luminescence intensity in the weak and strong excitation limits can now be written as

$$F_{weak} = \frac{F_{d4} F_{Fd2} F_a^2}{F_{Bd2} F_p^n} \qquad (12) \qquad F_{strong} = F_a \qquad (13)$$

where F_{Fd2}, F_{Bd2}, and F_{d4} are the enhancement factors for the energy transfer processes represented by the coefficients c_{Fd2}, c_{Bd2}, and c_{d4}, respectively, F_a is the absorption enhancement factor, and F_p is the Purcell factor, which is the enhancement factor for the radiative decay rate. The exponent, n, for the Purcell factor in eq 12 is either 0 or 2, depending on whether the donor decay is dominated by nonradiative or radiative channels. According to eq 13, the enhancement in the strong excitation limit is entirely due to the absorption enhancement. From Figure 4c, the enhancement factors for the green and red emission in the strong excitation limit are 3.1 and 4.2, respectively. Ideally, the enhancement factors should be the same for both green and red emissions. The discrepancy is attributed to the red emission excited by the three-photon processes, which could become non-

negligible in the strong excitation limit but are not included in our rate equation analysis. We therefore consider the enhancement factor for the green emission to be the more accurate value for the absorption enhancement, $F_a = 3.1$. Since the time-averaged absorbed power is given by $U_a = (1/2)\int\omega\varepsilon''|\mathbf{E}|^2 dV$,(51) where ε'' is the imaginary part of the permittivity, the absorption enhancement can be calculated numerically by comparing the $|\mathbf{E}|^2$integrated over the UCNP layer. For this, we obtained the steady state field distribution at 980 nm as shown in the inset of Figure 2. The field profile shows surface plasmon modes with enhanced local field strength. The resultant absorption enhancement in the UCNP layer on nanograting structure compared to the reference sample on flat silver film was 2.8, which was in good agreement with the experimentally observed green enhancement factor in the strong excitation limit and thus offers strong support for our assertion that the green enhancement is due entirely to the absorption enhancement.

We now turn our attention to eqs 8 and 12 for the green emission in the weak excitation limit. Since the green emission rate has quadratic dependence on the incident power, the overall enhancement factor should depend on F_a^2. For the donor decay rate W_{D10} in eq 8, Figure 5b showed the decay rate is determined mainly by the nonradiative decay rate with an effective lifetime of around 200 μs which is over 8 times smaller than the radiative decay time of UCNP on glass substrate. Therefore, the decay processes will remain predominantly nonradiative even if there is a modest increase in radiative decay rate by the Purcell effect. As discussed later, the Purcell factor is close to unity in our system. The value of W_{D10} would therefore remain unaffected by the plasmon resonance, and we choose $n = 0$ in eq 12. Since the branching ratio, W_{A40}/W_{A4}, and the doping densities, N_D and N_A, should be independent of the excitation power, the only remaining factors in eq 8 are the energy-transfer coefficients, c_{Fd2}, c_{Bd2}, and c_{d4}, whose enhancement factors are denoted as F_{Fd2}, F_{Bd2}, and F_{d4} in eq 12. Since the experimental data tell us $F_{strong} = 3.1$ and $F_{weak} = 16.0$, we find $F_{Fd2}F_{d4}/F_{Bd2} = 1.7$.

To continue the discussion on the enhancement factors for the energy transfer coefficients, we consider the Förster energy transfer rate for a donor–acceptor pair in a dispersive and absorbing medium given by

$$W_{ET} = \int d\omega \sigma_A(\omega)\sigma_D(\omega)\tilde{w}(\omega) \qquad (14)$$

where σ_A and σ_D are the free-space absorption and emission spectra of acceptor and donor, respectively.(51, 56, 60) The information about the medium is contained in $\tilde{w}(\omega)$, which can be expressed in terms of the dyadic Green function as follows.

$$\tilde{w}(\omega) = \frac{2\pi\omega^2}{\hbar^2\varepsilon_0 c^2}\left|\mathbf{d}_A^* \cdot \mathbf{G}(\mathbf{r}_A, \mathbf{r}_D, \omega) \cdot \mathbf{d}_D\right|^2 \qquad (15)$$

Here, $\mathbf{d}_A$ and $\mathbf{d}_D$ are the dipole moments of acceptor and donor respectively; $\mathbf{r}_A$ and $\mathbf{r}_D$ indicate the positions of acceptor

and donor, respectively. Using this formalism, it has been shown theoretically that the Förster energy transfer rate can be enhanced near the plasmon resonance.(51, 52, 57) The rigorous evaluation of the dyadic Green function is nontrivial and the theoretical works have so far been carried out mostly for highly symmetric shapes like planar surface, sphere, and ellipsoid.(51-55, 58, 59) A previous study observed enhanced Förster energy transfer rate in optical cavities and attributed it to the enhanced local density of states (LDOS) to which the donor emission rate is directly proportional.(51, 52, 56) In terms of the dyadic Green function, however, the emission rate of a dipole is given by

$$W_{SE} = \frac{2\omega^2}{\hbar\varepsilon_0 c^2}[\mathbf{d}_D^* \cdot \mathrm{Im}\,\mathbf{G}(\mathbf{r}_D, \mathbf{r}_D, \omega) \cdot \mathbf{d}_D] \quad (16)$$

where Im indicates the imaginary part.(9, 57, 60-65) For a small donor–acceptor distance, $\mathbf{G}(\mathbf{r}_A,\mathbf{r}_D,\omega)$, may be similar to $\mathbf{G}(\mathbf{r}_D,\mathbf{r}_D,\omega)$. However, the real part of the dyadic Green function often dominates over the imaginary part, and thus, the energy-transfer enhancement is generally quite different from the emission enhancement. In fact, it has recently been shown that the energy-transfer enhancement is not related to the LDOS enhancement.(58, 59, 66) The theoretical studies indicate that the energy-transfer enhancement is generally much smaller than the spontaneous emission enhancement.(51, 52, 67) Nevertheless, it has been experimentally observed that the Förster energy transfer rate can be significantly enhanced in the vicinity of plasmonic structures.(9, 60-65)

In order to properly describe the effect of energy transfer on the upconversion process in the UCNP where the donor density is very high, we must consider energy transfer among donors. For multipolar interaction mechanism, the energy transfer rate between a donor and an acceptor separated by a distance, r, is given by(66)

$$W_{ET}(r) = \frac{1}{\tau_R}\left(\frac{r_0}{r}\right)^s \quad (17)$$

where r_0 is the Förster radius defined as the distance at which the energy transfer rate becomes equal to the radiative decay rate, τ_R is the radiative lifetime of the donor, and s = 6, 8, 10, ... for dipole–dipole, dipole–quadrupole, and quadrupole–quadrupole interaction, respectively. Taking into account the energy migration over donors, the statistical average of the probability of finding a donor in the excited state at time t is given by(67)

$$\phi(t) = \exp\left[-\frac{t}{\tau_R} - \Gamma\left(1 - \frac{3}{s}\right)\frac{N_A}{N_0}\left(\frac{t}{\tau_R}\right)^{3/s}\right] \quad (18)$$

where N_A is the acceptor density and N_0 is the critical density defined as $N_0 = 3/(4\pi r_0^3)$. The second term in the exponent in eq 18 represents the nonexponential decay due to the energy migration over donors and the eventual energy transfer to an acceptor. An effective energy transfer time, τ_e, can now be defined as the time the probability function decays to the e^{-1} point

$$\tau_e = \frac{\tau_R}{\pi}\left(\frac{N_0}{N_A}\right)^2 \quad (19)$$

for dipole–dipole coupling, $s = 6$. Or the effective energy

$$\frac{1}{\tau_e} = \frac{\pi}{\tau_R}\left(\frac{N_A}{N_0}\right)^2 = \frac{\pi}{\tau_R}\left(\frac{r_0}{r_A}\right)^6$$

transfer rate can be written as $= \pi W_{ET}(r_A)$ (20) where r_A is defined similarly to r_0, $N_A = 3/(4\pi r_A^3)$. Thus, in a system like our UCNP where the energy migration over donors may be significant, the effective rate of energy transfer rate from an excited donor to an acceptor is proportional to the Förster energy transfer rate for an isolated donor–acceptor pair separated by r_A, the effective distance between two adjacent acceptors.

This effective rate of energy transfer can now be related to the energy-transfer coefficients used in the rate equations where the rates of forward transfer from $^2F_{5/2}(Yb^{3+})$ to $^4I_{11/2}(Er^{3+})$, backward transfer from $^4I_{11/2}(Er^{3+})$ to $^2F_{5/2}(Yb^{3+})$, and upconversion transfer from $^2F_{5/2}(Yb^{3+})$ to $^4F_{7/2}(Er^{3+})$ are represented by $c_{Fd2}N_{A0}$, $c_{Bd2}N_{D0}$, and $c_{d4}N_{A2}$, respectively. In the weak excitation limit where the energy transfer rate enhancement is relevant according to eqs 12 and 13, we have $N_{A0} = N_A$ and $N_{D0} = N_D$ and thus write

$$c_{Fd2}N_A = \pi W_{ET}(r_A), \quad r_A = \sqrt[3]{\frac{3}{4\pi N_A}}$$
$$c_{Bd2}N_D = \pi W_{ET}(r_D), \quad r_D = \sqrt[3]{\frac{3}{4\pi N_D}}$$
$$c_{d4}N_{A2} = \pi W_{ET}(r_{A2}), \quad r_{A2} = \sqrt[3]{\frac{3}{4\pi N_{A2}}} \quad (21)$$

Thus, to examine the enhancement of energy transfer coefficients, we can evaluate the energy transfer rates given by eq 14 at distances r_A, r_D, and r_{A2}, which are the effective distances for the ground-state acceptor, ground-state donor, and excited-state ($^4I_{11/2}$) acceptor, respectively. From the crystal structure data available in the literature, (68) we find $N_D = 1.98 \times 10^{21}$ cm^{-3} and $N_A = 2.2 \times 10^{20}$ cm^{-3} for doping densities of 18% Yb and 2% Er, and from these values we determine $r_D = 0.5$ nm and $r_A = 1.0$ nm. The density of excited acceptors, N_{A2}, is given by eq 14 in the Supporting Information. However, due to the uncertainties of the various parameter values, we make an approximate estimate by invoking a simple rate equation for a two-level system, which asserts that in the steady state the excitation rate should be equal to the decay rate. The decay rate is given by the measured decay time, $\tau = 200$ μs, from Figure 5b. The excitation rate is determined by the excitation power density and the absorption coefficient, $\alpha = 6$ cm^{-1}.(4) Since we are concerned with the weak excitation regime, we use the excitation power density of 1 kW/cm^2 and find the excitation rate of 3×10^{22} cm^{-3} s^{-1}. Now the density of excited ions is found by

simply multiplying the excitation rate with the decay time, $N_{A2} = 6 \times 10^{18}$ cm^{-3}, which subsequently yields $r_{A2} = 3.4$ nm.

Evaluating the energy transfer rate from eq 14 calls for numerically calculating the dyadic Green function. Unfortunately, this is extremely challenging especially for small donor–acceptor distances as the real part of the Green function becomes very large. Therefore, instead of directly evaluating the energy transfer rate in the nanograting structure, we conducted model calculations for the energy transfer rates near a flat metal surface for which analytical solutions exist.(51) As shown in the data presented in the Supporting Information, the Förster energy transfer rates are enhanced at frequencies slightly below the surface plasmon frequency. The enhancement is larger for donor–acceptor pairs placed closer to the metal surface and also for larger donor–acceptor separation distances. The enhancement also depends on the orientations of the donor and acceptor dipole moments. However, in no cases do we observe any enhancement for extremely short donor–acceptor distance of 1 nm or shorter. It is therefore reasonable to assume there is no enhancement in c_{Fd2} and c_{Bd2} or $F_{Fd2} = F_{Bd2} = 1$. We may then further simplify eq 12 to

$$F_{weak} = F_{d4} F_a^2 \qquad (22)$$

and find the enhancement factor for the energy transfer upconversion process to be $F_{d4} = 1.7$. This result is considered reasonable because the enhancement calculated for a flat metal surface in the Supporting Information shows significant enhancements are possible for a donor–acceptor placed $0.03\lambda_{sp}$ away from metal surface with donor–acceptor distance of 3–4 nm, which corresponds to our estimate of r_{A2}. Our argument is also consistent with the literature which showed the enhancement of Förster energy transfer rate is larger for larger donor–acceptor distances.(1, 5, 53) In particular, a recent theoretical study on the Förster energy transfer rates in the vicinity of metallic nanoparticle showed that the Förster energy transfer rates remain mostly unperturbed for short donor–acceptor distances but strongly modified for large donor–acceptor distances.(52) This behavior is understood by considering the two components that contribute to the Green function: direct emission of donor dipole and the reflection from the metal surface. For short distances, the former dominates and the Förster energy transfer rate remains the same. For larger distances, the latter begins to make a significant contribution and the resultant interference between the two components gives rise to the increase or decrease in the Förster energy transfer rate. In our case, the contribution by the metal surface becomes significant enough to result in an enhanced Förster energy transfer rate only for the upconversion energy transfer from $^2F_{5/2}(Yb^{3+})$ to $^4F_{7/2}(Er^{3+})$.

Finally, we discuss the Purcell factor, which describes the enhancement of donor radiative decay rate due to the increased LDOS.(69, 70) The Purcell factor depends on the quality factor and mode

volume.(38) The plasmonic grating used in this study has a large mode volume and tends to exhibit small Purcell factor.(71) To precisely evaluate the Purcell factor, we followed the method by Gong *et al.*(71) and obtained $F_p = 1.78$. The details of the calculation are given in the Supporting Information. It is worth mentioning that a recent study showed the Purcell factor is not equal to the acceleration of radiative decay in plasmonic systems.(72) To check this, we numerically calculated the radiation rate of a point dipole using finite-difference time-domain method. Comparing the radiation rates on a nanograting and in free space, we found an enhancement of 1.8, which agrees well with the independently calculated Purcell factor. We thus conclude the Purcell effect accurately describes the donor emission enhancement in our system. The small Purcell factor validates the use of n = 0 in eq 12 to derive eq 22 as the nonradiative processes should dominate the decay of $^2F_{5/2}$ (D1) level. Based on this analysis, we may conclude the absorption and Förster energy transfer are the two processes contributing to the enhancement of luminescence upconversion. In the strong excitation limit, only absorption enhancement accounts for the entire upconversion enhancement while in the weak excitation limit both the Förster energy transfer and absorption enhancements contribute. Overall, absorption enhancement plays the most important role in the upconversion enhancement.

Conclusions

In conclusion, we report a comprehensive experimental and analytical study on the plasmon enhancement of ETU process in $NaYF_4:Yb^{3+},Er^{3+}$ nanoparticles. As a nonlinear process, upconversion is inherently sensitive to the excitation power. Consequently, the enhancement of the upconversion process by surface plasmons is also highly sensitive to the excitation condition and the PL intensity enhancement may vary widely under different excitation power densities. Thus, it is imperative to specify and identify whether the measurements were taken in the weak, intermediate or strong excitation regimes. The upconverted luminescence intensity was found to depend quadratically on the excitation power in the weak excitation limit and linearly in the strong excitation limit. This general behavior is preserved in the presence of surface plasmon except that curves are shifted to the lower power densities, which is indicative of the enhanced local electromagnetic energy density due to surface plasmon. We then conducted an analysis based on the rate equations governing the upconversion process and derived simple expressions for the enhancement factors for the weak and strong excitation regimes. It was found that the enhancement in the strong excitation regime is entirely due to the absorption enhancement and any possible enhancements in Förster energy transfer rate and radiative decay rate do not contribute. In the weak excitation regime, both

absorption enhancement and enhancement of Förster energy transfer rate contribute. Thus, in summary, we identified two main mechanisms contributing to the plasmon enhancement of luminescence upconversion, absorption and energy transfer. The absorption enhancement is described by the Maxwell's equations while the energy transfer obeys the Förster's theory. The absorption enhancement plays the dominant role while the energy transfer enhancement is small and is effective only in the weak excitation regime. In the end, we derived simple expressions for the overall enhancement factors for the upconverted luminescence intensity in the weak and strong excitation limits. Our work sheds light on how surface plasmon enhances the ETU process in rare-earth based upconversion materials and allows meaningful comparisons among the widely varying reports in the literature. It also offers a firm foundation for more advanced engineering of plasmon enhanced upconversion materials.

Methods

UCNP Synthesis

UCNPs were synthesized using a modified coprecipitation method(22) where 0.3 g of YCl_3, 0.1 g of $YbCl_3$, and 0.01 g of $ErCl_3$ were dissolved into 36 mL of octadecene and 6 mL of oleic acid with vigorous stirring and heating. Then a mixture of 0.2 g of NaOH and 0.296 g of NH_4F in 20 mL of methanol was added and vigorously stirred for 30 min at 60 °C. After 30 min, the mixture was heated to 100 °C for degassing. Then, the mixture was heated to 320 °C for 1 h under argon atmosphere. Once the final product had cooled, the mixture was washed in water and ethanol *via*centrifugation and redispersion. After a final step of washing, UCNPs were stored in toluene.

UCNP Surface Modification

Since the as-synthesized UCNPs are covered with oleic acid and thus insoluble to water, further modification is necessary to make the particles water-soluble and also to produce surface charge for the subsequent layer-by-layer deposition. For this purposed, we followed the method reported in the literature.(73, 74) Methoxyethylamine (EtOMe) was covalently bound to poly(maleic anhydride-*alt*-1-octadecene) (PMAO) to make PMAO amphiphilic. Then the polymer is attached on the UCNP surface by the hydrophobic interaction between the surfactant on the UCNP surface and the hydrophobic portion of the amphiphilic polymer while the hydrophilic part of PMAO makes the UCNPs water-soluble. The PMAO also turns the UCNP surface negatively charged due to hydrolyzed carboxyl groups.(74) Specifically, the as-synthesized UCNPs in toluene were centrifuged

at 12 kG for 60 min, decanted, and redispersed in chloroform. Separately, 80 mg of PMAO and 28 μL of EtOMe were added to 2 mL of chloroform. Then, the UCNPs in chloroform were added to the mixture of PMAO and EtOMe and stirred for 20 min. Afterward, the UCNP, PMAO, and EtOMe mixture in chloroform was transferred to a round-bottomed flask and dried in vacuum overnight. Following the drying process, 50 mL of distilled and deionized water (DDH_2O) was added to the flask, and the mixture was vigorously stirred for 3 h. Then the solution was sonicated for more than 5 h and washed *via* centrifugation and redispersion. Final concentration of UCNP was adjusted to be 10 mg/mL.

Nanograting Fabrication

To fabricate the silver nanograting structure, we used nanoimprint lithography. A 200 nm thick Ag film was deposited on a silicon substrate coated with a 20 nm thick Cr adhesion layer. Another 10 nm thick Au layer was deposited on top to prevent any oxidation of silver during the subsequent oxygen reactive ion etching (RIE) process. Then, a 175 nm thick poly(methyl methacrylate) (PMMA) layer was spin-coated and baked on a hot plate. A silicon mold with a grating structure (LightSmyth Technologies) was used to imprint the PMMA layer and the oxygen RIE was carried out to remove any residual PMMA in the trenches. By evaporating a 20 nm thick Ag film on top of the imprinted PMMA layer and lifting off in acetone, a high-quality silver grating structure was obtained over a large area (0.64 mm^2). Finally, a thin Si_3N_4 layer was deposited on the silver gratings by plasma-enhanced chemical vapor deposition to alleviate luminescence quenching.

Layer-by-Layer Deposition of UCNPs

The layer-by-layer (LBL) deposition process driven by the electrostatic interaction was carried out by using polyelectrolytes as intermediaries.(75-77) Si_3N_4-coated silver nanogratings were washed in acetone overnight and dried in vacuum oven for 3 h. The cleaned nanogratings were then immersed in 1% (v/v) (3-aminopropyl)triethyoxysilane (APTS) in toluene for 3 h. Then the nanogratings were washed with toluene and ethanol and dried in vacuum oven overnight. The APTS-coated chips were then stamped with a silicone glue well (diameter ~4 mm) to define the area of nanoparticle deposition. After the silicone glue well was dried for 20 min, 6 μL of surface-modified UCNP solution was drop-cast and allowed to react for 20 min. A gentle washing to get rid of unbound nanoparticles was then performed. Then, 6 μL of 2 mg/mL of poly(allylamine hydrochloride) (PAH) solution was drop-cast in the well, reacted for 20 min, and gently washed. These procedures were repeated until three monolayers of UCNPs were obtained. Successful deposition of three monolayers in the layer-by-layer fashion was confirmed by the atomic force microscopy performed at each layer. The final thickness of three monolayers was measured to be 90 nm by the atomic force microscopy.

Optical Spectroscopy

We measured the reflectance spectrum of the nanogratings using a spectrometer (Acton SpectraPro 300i) with cooled charge-coupled device (CCD) detectors. A tungsten lamp was used as the light source. The incident light was polarized in the direction orthogonal to grating lines to excite the surface plasmon modes. The incident light was directed to the sample through a beam splitter cube at normal incidence. A collimating lens with focal length of 5 cm was used to collect reflected light from the sample. The collimated light was then refocused onto the spectrometer input slit with a numerical aperture matched focusing lens. A liquid nitrogen cooled Si CCD (Roper Scientific) and a thermoelectric cooled InGaAs CCD (Andor) were used to detect and record the visible and near-infrared spectrum, respectively. The source spectrum was measured in exactly the same way but the sample replaced by a highly reflective mirror for calibration.

The photoluminescence spectroscopy was conducted by the same collection optics and spectrometer with the reflectance spectroscopy. The excitation source was a 980 nm laser diode (OEM laser). A clean up filter (Semrock LL01–980) with bandwidth of 3.7 nm was used to remove laser tail outside central laser wavelength. A dichroic mirror was used to direct the laser beam onto the sample at normal incidence while transmitting the visible photoluminescence signal from the UCNPs. The visible emission was focused onto spectrometer by the collection optics and detected by a liquid nitrogen cooled Si CCD detector. Similarly, the NIR emission spectrum is measured with an NIR beam splitter and InGaAs CCD detector. In order to protect the detector from the excitation laser, one long-pass edge filter (Semrock BLP01-980R) was used.

For time-resolved photoluminescence spectroscopy, a pulsed 980 nm laser was used to excite UCNP samples at normal incidence. The pulse shape and duration were controlled by a function generator (Wavetak) that controlled the laser diode current driver (Thorlabs, TCLDM9). The optics were exactly the same as for the NIR photoluminescence spectroscopy except that a monochromator (Sciencetech 9057F) equipped with an NIR photomultiplier tube (Hamamatsu H10330B-75), which is connected to a photon counter (Stanford Research Systems SR430), was used. The photon counter input was synchronized with the laser pulse by function generator, and the decay curve was stored in the internal memory of photon counter.

Finite Element Modeling

We modeled the UCNP layers on nanograting and flat metal surface (the reference sample) using the commercially available software COMSOL Multiphysics. The structural parameters used in the simulations were extracted from the SEM images. The nanograting period is 829 nm with a grating line width of 410 nm and a height of 10 nm. On the nanograting or flat metal surface, we have a 30

nm thick Si_3N_4 layer and then a 90 nm thick UCNP layers. The gold and silver dielectric functions were based on the experimentally measured values(24) with increased imaginary parts to account for the increased electron scattering in nanostructured materials.(25) The Si_3N_4 and UCNP were treated as lossless dielectric with refractive indices of 2 and 1.3, respectively.(78) $NaYF_4$ has a refractive index of 1.4.(12) In our case, we have a loosely packed nanoparticle layer, not a continuous film. We thus used a slightly smaller refractive index value. It should also be noted that the absorption of $NaYF_4$:Yb^{3+},Er^{3+} is weak (absorption coefficient $\alpha = 6\ cm^{-1}$),(5) therefore modeling it as a lossless dielectric material yields accurate field profiles.

To obtain a reflectance spectrum, a unit cell of nanograting or a planar metal surface with the same length was illuminated with normally incident plane wave with polarization along the direction of grating periodicity. The computational cell was terminated with periodic boundary conditions along the direction of periodicity. The reflected power was then calculated as a function of frequency to obtain reflectance spectrum. The same simulation also provided steady-state field profiles, which were used to calculate the absorption enhancement. As described in the text, the absorption enhancement was calculated by taking the ratio of integrated squared amplitude of electric field over the UCNP layer. The same field profile was also used to calculate the Purcell factor following the method by Gong *et al.*(71) of which the details are provided in the Supporting Information.

The emission patterns of the naongrating and reference samples were also obtained from COMSOL modeling. Basically, we put a dipole source with emission wavelength of 550 nm (UCNP green emission band) at the center of UCNP layer and calculated the emitted power within the solid angle captured by our collection lens (NA = 0.13) used in PL measurements. To take into account the random polarization of UCNP emission, we repeated this calculation over different dipole polarization orientations with 15° intervals and obtained an average. The difference was negligibly small, ~4%.

Supporting Information

Thickness measurement data for the LBL UCNP layers, details of solving rate equations under weak and strong excitation limit, the visible luminescence decay measurement results, and details of Purcell factor calculation. This material is available free of charge *via* the Internet at http://pubs.acs.org.

- **PDF**
  - nn5011254_si_001.pdf (1.1 MB)

Plasmon Enhancement Mechanism for the Upconversion Processes in $NaYF_4:Yb^{3+},Er^{3+}$ Nanoparticles: Maxwell *versus* Förster

figshare

ShareDownload

The authors declare no competing financial interest.

Acknowledgment

This work was supported by the National Science Foundation through Grant CHE-1125935.

Reference QuickView

References

This article references 78 other publications.

1. 1.

Franken, P.; Hill, A.; Peters, C.; Weinreich, G. Generation of Optical Harmonics *Phys. Rev. Lett.* **1961**, 7,118– 119

[Crossref]

2. 2.

Auzel, F. Upconversion Processes in Coupled Ion Systems *J. Lumin.* **1990**, 45, 341– 345

[Crossref], [CAS]

3. 3.

Auzel, F. Upconversion and Anti-Stokes Processes with F and D Ions in Solids *Chem. Rev.* **2004**, 104, 139–174

[ACS Full Text], [CAS]

4. 4.

Page, R. H.; Schaffers, K. I.; Waide, P. A.; Tassano, J. B.; Payne, S. A.; Krupke, W. F.; Bischel, W. K.Upconversion-Pumped Luminescence Efficiency of Rare-Earth-Doped Hosts Sensitized with Trivalent Ytterbium *J. Opt. Soc. Am. B* **1998**, 15, 996– 1008

[Crossref], [CAS]

5. 5.

Shpaisman, H.; Niitsoo, O.; Lubomirsky, I.; Cahen, D. Can Up- and Down-Conversion and Multi-Exciton Generation Improve Photovoltaics? *Sol. Energy Mater. Sol. Cells* **2008**, 92, 1541– 1546

[Crossref], [CAS]

6. 6.

Nie, S.; Emory, S. R. Probing Single Molecules and Single Nanoparticles by Surface-Enhanced Raman Scattering *Science* **1997**, 275, 1102– 1106

[Crossref], [PubMed], [CAS]

7. 7.

Michaels, A. M.; Nirmal, M.; Brus, L. E. Surface Enhanced Raman Spectroscopy of Individual Rhodamine 6G Molecules on Large Ag Nanocrystals *J. Am. Chem. Soc.* **1999**, 121, 9932– 9939

[ACS Full Text], [CAS]

8. 8.

Lakowicz, J. R. Radiative Decay Engineering 5: Metal-Enhanced Fluorescence and Plasmon Emission *Anal. Biochem.* **2005**, 337, 171– 194

[Crossref], [PubMed], [CAS]

9. 9.

Andrew, P. Energy Transfer Across a Metal Film Mediated by Surface Plasmon Polaritons *Science* **2004**,306, 1002– 1005

[Crossref], [PubMed], [CAS]

10. 10.

Lunz, M.; Gerard, V. A.; Gun'ko, Y. K.; Lesnyak, V.; Gaponik, N.; Susha, A. S.; Rogach, A. L.; Bradley, A. L.Surface Plasmon Enhanced Energy Transfer Between Donor and Acceptor CdTe Nanocrystal Quantum Dot Monolayers *Nano Lett.* **2011**, 11, 3341– 3345

[ACS Full Text], [CAS]

11. 11.

Esteban, R.; Laroche, M.; Greffet, J. J. Influence of Metallic Nanoparticles on Upconversion Processes *J. Appl. Phys.* **2009**, 105, 033107

[Crossref], [CAS]

12. 12.

Saboktakin, M.; Ye, X.; Chettiar, U. K.; Engheta, N.; Murray, C. B.; Kagan, C. R. Plasmonic Enhancement of Nanophosphor Upconversion Luminescence in Au Nanohole Arrays *ACS Nano* **2013**, 7, 7186– 7192

[ACS Full Text], [CAS]

13. 13.

Yuan, P.; Lee, Y. H.; Gnanasammandhan, M. K.; Guan, Z.; Zhang, Y.; Xu, Q.-H. Plasmon Enhanced Upconversion Luminescence of $NaYF_4$:Yb,Er@SiO_2@Ag Core–Shell Nanocomposites for Cell Imaging*Nanoscale* **2012**, 4, 5132

[Crossref], [CAS]

14. 14.

Zhang, W.; Ding, F.; Chou, S. Y. Large Enhancement of Upconversion Luminescence of $NaYF_4$:Yb^{3+}/Er^{3+}Nanocrystal by 3D Plasmonic Nano-Antennas *Adv. Mater.* **2012**, 24, OP236– OP241

[Crossref]

15. 15.

Li, Z. Q.; Chen, S.; Li, J. J.; Liu, Q. Q.; Sun, Z.; Wang, Z. B.; Huang, S. M. Plasmon-Enhanced Upconversion Fluorescence in $NaYF_4$:Yb/Er/Gd Nanorods Coated with Au Nanoparticles or Nanoshells *J. Appl. Phys.* **2012**, 111, 014310

[Crossref], [CAS]

16. 16.

Paudel, H. P.; Zhong, L.; Bayat, K.; Baroughi, M. F.; Smith, S.; Lin, C.; Jiang, C.; Berry, M. T.; May, P. S.Enhancement of Near-Infrared-to-Visible Upconversion Luminescence Using Engineered Plasmonic Gold Surfaces *J. Phys. Chem. C* **2011**, 115, 19028– 19036

[ACS Full Text], [CAS]

17. 17.

Deng, W.; Sudheendra, L.; Zhao, J.; Fu, J.; Jin, D.; Kennedy, I. M.; Goldys, E. M. Upconversion in $NaYF_4$:Yb, Er Nanoparticles Amplified by Metal Nanostructures *Nanotechnology* **2011**, 22,325604

[Crossref], [PubMed], [CAS]

18. 18.

Liu, N.; Qin, W.; Qin, G.; Jiang, T.; Zhao, D. Highly Plasmon-Enhanced Upconversion Emissions From Au@β-$NaYF_4$:Yb,Tm Hybrid Nanostructures *Chem. Commun.* **2011**, 47, 7671– 7673

[Crossref], [PubMed], [CAS]

19. 19.

Zhang, H.; Li, Y.; Ivanov, I. A.; Qu, Y.; Huang, Y.; Duan, X. Plasmonic Modulation of the Upconversion Fluorescence in $NaYF_4$:Yb/Tm Hexaplate Nanocrystals Using Gold Nanoparticles or Nanoshells *Angew. Chem., Int. Ed.* **2010**, 49, 2865– 2868

[Crossref], [PubMed], [CAS]

20. 20.

Schietinger, S.; Aichele, T.; Wang, H.-Q.; Nann, T.; Benson, O. Plasmon-Enhanced Upconversion in Single $NaYF_4$:Yb^{3+}/Er^{3+} Codoped Nanocrystals *Nano Lett.* **2010**, 10, 134– 138

[ACS Full Text], [CAS]

21. 21.

Zhang, H.; Xu, D.; Huang, Y.; Duan, X. Highly Spectral Dependent Enhancement of Upconversion Emission with Sputtered Gold Island Films *Chem. Commun.* **2010**, 47, 979– 981

[Crossref], [PubMed]

22. 22.

Li, Z.; Zhang, Y. An Efficient and User-Friendly Method for the Synthesis of Hexagonal-Phase $NaYF_4$:Yb, Er/Tm Nanocrystals with Controllable Shape and Upconversion Fluorescence *Nanotechnology* **2008**, 19,345606

[Crossref], [PubMed], [CAS]

23. 23.

Holmgaard, T.; Bozhevolnyi, S. Theoretical Analysis of Dielectric-Loaded Surface Plasmon-Polariton Waveguides *Phys. Rev. B* **2007**, 75, 245405

[Crossref], [CAS]

24. 24.

Johnson, P. B.; Christy, R. W. Optical Constants of the Noble Metals *Phys. Rev. B* **1972**, 6, 4370

[Crossref], [CAS]

25. 25.

Drachev, V. P.; Chettiar, U. K.; Kildishev, A. V.; Yuan, H.-K.; Cai, W.; Shalaev, V. M. The Ag Dielectric Function in Plasmonic Metamaterials *Opt. Express* **2008**, 16, 1186– 1195

[Crossref], [PubMed], [CAS]

26. 26.

Kingsley, J. D. Analysis of Energy Transfer and Infrared-to-Visible Conversion in LaF_3:Yb,Er *J. Appl. Phys.***1970**, 41, 175

[Crossref], [CAS]

27. 27.

Johnson, L. F. Infrared-to-Visible Conversion by Rare-Earth Ions in Crystals *J. Appl. Phys.* **1972**, 43,1125

[Crossref], [CAS]

28. 28.

Mita, Y. Luminescence Processes in Yb^{3+}-Sensitized Rare-Earth Phosphors *J. Appl. Phys.* **1972**, 43, 1772–1778

[Crossref], [CAS]

29. 29.

Wright, J. C. Up-Conversion and Excited State Energy Transfer in Rare-Earth Doped Materials. In*Radiationless Processes in Molecules and Condensed Phases*; Springer: Berlin, **1976**; pp 239– 295.

[Crossref]

30. 30.

Mai, H. X.; Zhang, Y. W.; Sun, L. D.; Yan, C. H. Highly Efficient Multicolor Up-Conversion Emissions and Their Mechanisms of Monodisperse $NaYF_4$:Yb,Er Core and Core/Shell-Structured Nanocrystals *J. Phys. Chem. C* **2007**, 111, 13721– 13729

[ACS Full Text], [CAS]

31. 31.

Yu, X.; Summers, C. J.; Park, W. Controlling Energy Transfer Processes and Engineering Luminescence Efficiencies with Low Dimensional Doping *J. Appl. Phys.* **2012**, 111, 073524

[Crossref], [CAS]

32. 32.

Dong, B.; Cao, B.; Feng, Z.; Wang, X.; Li, C.; Hua, R. Up-Conversion Emissions of Er^{3+}-Yb^{3+} Codoped Al_2O_3 Nanoparticles by the Arc Discharge Synthesis Method *Sci. China, Ser. G: Phys., Mech. Astron.* **2009**,52, 1043– 1046

[Crossref], [CAS]

33. 33.

Strohhöfer, C.; Polman, A. Relationship Between Gain and Yb^{3+} Concentration in Er^{3+}–Yb^{3+} Doped Waveguide Amplifiers *J. Appl. Phys.* **2001**, 90, 4314– 4320

[Crossref], [CAS]

34. 34.

Suyver, J.; Aebischer, A.; García-Revilla, S.; Gerner, P.; Güdel, H. Anomalous Power Dependence of Sensitized Upconversion Luminescence *Phys. Rev. B* **2005**, 71, 125123

[Crossref], [CAS]

35. 35.

Kingsley, J. D.; Fenner, G. E.; Galginaitis, S. V. Kinetics and Efficiency of Infrared-to-Visible Conversion in LaF_3:Yb,Er *Appl. Phys. Lett.* **2003**, 15, 115– 117

[Crossref]

36. 36.

Sommerdijk, J. On the Excitation Mechanisms of the Infrared-Excited Visible Luminescence in Yb^{3+}, Er^{3+}-Doped Fluorides *J. Lumin.* **1971**, 4, 441– 449

[Crossref], [CAS]

37. 37.

Chen, D.; Wang, Y.; Ma, E.; Yu, Y.; Liu, F. Partition, Luminescence and Energy Transfer of Er^{3+}/Yb^{3+} Ions in Oxyfluoride Glass Ceramic Containing CaF_2 Nano-Crystals *Opt. Mater.* **2007**, 29, 1693– 1699

[Crossref], [CAS]

38. 38.

Florea, C.; Winick, K. A. Ytterbium-Doped Glass Waveguide Laser Fabricated by Ion Exchange *J. Lightwave Technol.* **1999**, 17, 1593– 1601

[Crossref], [CAS]

39. 39.

Taccheo, S.; Sorbello, G.; Longhi, S.; Laporta, P. Measurement of the Energy Transfer and Upconversion Constants in Er–Yb-Doped Phosphate Glass *Opt. Quantum Electron.* **1999**, 31, 249– 262

[Crossref], [CAS]

40. 40.

Winick, K. A.; Vossler, G. L. Erbium: Ytterbium Planar Waveguide Laser in Ion-Exchanged Glass *Proc. SPIE***1997**, 121– 134

[Crossref], [CAS]

41. 41.

Chamarro, M. A.; Cases, R. Infrared to Visible Upconversion of Er^{3+} Ions in Yb^{3+} Doped Fluorohafnate Glasses *J. Lumin.* **1990**, 46, 59– 65

[Crossref], [CAS]

42. 42.

Yeh, D. C.; Sibley, W. A.; Suscavage, M.; Drexhage, M. G. Multiphonon Relaxation and Infrared-to-Visible Conversion of Er^{3+} and Yb^{3+} Ions in Barium-Thorium Fluoride Glass *J. Appl. Phys.* **1987**, 62, 266–275

[Crossref], [CAS]

43. 43.

Cantelar, E.; Muñoz, J. A.; Sanz-García, J. A.; Cusso, F. Yb^{3+} to Er^{3+} Energy Transfer in $LiNbO_3$ *J. Phys.: Condens. Matter* **1998**, 10, 8893– 8903

[Crossref], [CAS]

44. 44.

Simondi-Teisseire, B. Yb^{3+} to Er^{3+} Energy Transfer and Rate-Equations Formalism in the Eye Safe Laser Material Yb:Er:$Ca_2Al_2SiO_7$ *Opt. Mater.* **1996**, 6, 267– 274

[Crossref], [CAS]

45. 45.

Sun, Q.-C.; Mundoor, H.; Ribot, J. C.; Singh, V.; Smalyukh, I. I.; Nagpal, P. Plasmon-Enhanced Energy Transfer for Improved Upconversion of Infrared Radiation in Doped-Lanthanide Nanocrystals *Nano Lett.***2014**, 14, 101– 106

[ACS Full Text], [CAS]

46. 46.

Nilsson, J.; Scheer, P.; Jaskorzynska, B. Modeling and Optimization of Short Yb^{3+}-Sensitized Er^{3+}-Doped Fiber Amplifiers *IEEE Photonics Technol. Lett.* **1994**, 6, 383– 385

[Crossref]

47. 47.

Hwang, B.-C.; Jiang, S.; Luo, T.; Watson, J.; Sorbello, G.; Peyghambarian, N. Cooperative Upconversion and Energy Transfer of New High Er^{3+}- and Yb^{3+}-Er^{3+}-Doped Phosphate Glasses *J. Opt. Soc. Am. B* **2000**,17, 833– 839

[Crossref], [CAS]

48. 48.

Zhao, J.; Lu, Z.; Yin, Y.; McRae, C.; Piper, J. A.; Dawes, J. M.; Jin, D.; Goldys, E. M. Upconversion Luminescence with Tunable Lifetime in $NaYF_4$:Yb,Er Nanocrystals: Role of Nanocrystal Size *Nanoscale***2013**, 5, 944– 952

[Crossref], [PubMed], [CAS]

49. 49.

Wyss, C.; Lüthy, W.; Weber, H. P.; Rogin, P.; Hulliger, J. Energy Transfer in Yb^{3+}:Er^{3+}:YLF *Opt. Commun.***1997**, 144, 31– 35

[Crossref], [CAS]

50. 50.

Cantelar, E.; Cusso, F. Dynamics of the Yb^{3+} to Er^{3+} Energy Transfer in $LiNbO_3$ *Appl. Phys. B: Lasers Opt.***1999**, 69, 29– 33

[Crossref], [CAS]

51. 51.

Dung, H. T.; Knöll, L.; Welsch, D.-G. Intermolecular Energy Transfer in the Presence of Dispersing and Absorbing Media *Phys. Rev. A* **2002**, 65, 043813

[Crossref], [CAS]

52. 52.

Gonzaga-Galeana, J. A.; Zurita-Sánchez, J. R. A Revisitation of the Förster Energy Transfer Near a Metallic Spherical Nanoparticle: (1) Efficiency Enhancement or Reduction? (2) The Control of the Förster Radius of the Unbounded Medium. (3) The Impact of the Local Density of States *J. Chem. Phys.* **2013**, 139,244302

[Crossref], [PubMed], [CAS]

53. 53.

Gersten, J. I.; Nitzan, A. Accelerated Energy Transfer Between Molecules Near a Solid Particle *Chem. Phys. Lett.* **1984**, 104, 31– 37

[Crossref], [CAS]

54. 54.

Hua, X. M.; Gersten, J. I.; Nitzan, A. Theory of Energy Transfer Between Molecules Near Solid State Particles *J. Chem. Phys.* **1985**, 83, 3650

[Crossref], [CAS]

55. 55.

Govorov, A.; Lee, J.; Kotov, N. Theory of Plasmon-Enhanced Förster Energy Transfer in Optically Excited Semiconductor and Metal Nanoparticles *Phys. Rev. B* **2007**, 76, 125308

[Crossref], [CAS]

56. 56.

Andrew, P.; Barnes, W. L. Förster Energy Transfer in an Optical Microcavity *Science* **2000**, 290, 785–788

[Crossref], [PubMed], [CAS]

57. 57.

Novotny, L.; Hecht, B. *Principles of Nano-Optics*; Cambridge University Press: Cambridge, **2012**.

[Crossref]

58. 58.

de Dood, M.; Knoester, J.; Tip, A.; Polman, A. Förster Transfer and the Local Optical Density of States in Erbium-Doped Silica *Phys. Rev. B* **2005**, 71, 115102

[Crossref], [CAS]

59. 59.

Blum, C.; Zijlstra, N.; Lagendijk, A.; Wubs, M.; Mosk, A. P.; Subramaniam, V.; Vos, W. L. Nanophotonic Control of the Förster Resonance Energy Transfer Efficiency *Phys. Rev. Lett.* **2012**, 109, 203601

[Crossref], [PubMed], [CAS]

60. 60.

Lunz, M.; Zhang, X.; Gerard, V. A.; Gun'ko, Y. K.; Lesnyak, V.; Gaponik, N.; Susha, A. S.; Rogach, A. L.;Bradley, A. L. Effect of Metal Nanoparticle Concentration on Localized

Surface Plasmon Mediated Förster Resonant Energy Transfer *J. Phys. Chem. C* **2012**, 116, 26529– 26534

[ACS Full Text], [CAS]

61. 61.

Zhou, Z.-K.; Li, M.; Yang, Z.-J.; Peng, X.-N.; Su, X.-R.; Zhang, Z.-S.; Li, J.-B.; Kim, N.-C.; Yu, X .-F.; Zhou, L.Plasmon-Mediated Radiative Energy Transfer Across a Silver Nanowire Array *via* Resonant Transmission and Subwavelength Imaging *ACS Nano* **2010**, 4, 5003– 5010

[ACS Full Text], [CAS]

62. 62.

Nakamura, T.; Fujii, M.; Miura, S.; Inui, M.; Hayashi, S. Enhancement and Suppression of Energy Transfer From Si Nanocrystals to Er Ions Through a Control of the Photonic Mode Density *Phys. Rev. B* **2006**, 74,045302

[Crossref], [CAS]

63. 63.

L Viger, M.; Brouard, D.; Boudreau, D. Plasmon-Enhanced Resonance Energy Transfer From a Conjugated Polymer to Fluorescent Multilayer Core–Shell Nanoparticles: a Photophysical Study *J. Phys. Chem. C* **2011**,115, 2974– 2981

[ACS Full Text], [CAS]

64. 64.

West, R. G.; Sadeghi, S. M. Enhancement of Energy Transfer Between Quantum Dots: the Impact of Metallic Nanoparticle Sizes *J. Phys. Chem. C* **2012**, 116, 20496– 20503

[ACS Full Text], [CAS]

65. 65.

Zhang, X.; Marocico, C. A.; Lunz, M.; Gerard, V. A.; Gun'ko, Y. K.; Lesnyak, V.; Gaponik, N.; Susha, A. S.;Rogach, A. L.; Bradley, A. L. Experimental and Theoretical Investigation of the Distance Dependence of Localized Surface Plasmon Coupled Förster Resonance Energy Transfer *ACS Nano* **2014**, 8, 1273–1283

[ACS Full Text], [CAS]

66. 66.

Förster, T. 10th Spiers Memorial Lecture. Transfer Mechanisms of Electronic Excitation *Discuss. Faraday Soc.* **1959**, 27, 7– 17

[Crossref]

67. 67.

Inokuti, M.; Hirayama, F. Influence of Energy Transfer by the Exchange Mechanism on Donor Luminescence*J. Chem. Phys.* **1965**, 43, 1978– 1989

[Crossref], [CAS]

68. 68.

Li, Z.; Park, W.; Zorzetto, G.; Lemaire, J. S. Synthesis Protocols for δ-Doped $NaYF_4$:Yb,Er *Chem. Mater.***2014**, 26, 1770– 1778

[ACS Full Text], [CAS]

69. 69.

Purcell, E. M. Spontaneous Emission Probabilities at Radio Frequencies *Phys. Rev.* **1946**, 69, 681

[Crossref]

70. 70.

Gérard, J.-M.; Gayral, B. Semiconductor Microcavities, Quantum Boxes and the Purcell Effect. In *Confined Photon Systems*; Lecture Notes in Physics; Springer: Berlin, **1999**; Vol. 531, pp 331– 351.

[Crossref]

71. 71.

Gong, Y.; Lu, J.; Cheng, S.-L.; Nishi, Y.; Vučković, J. Plasmonic Enhancement of Emission From Si-Nanocrystals *Appl. Phys. Lett.* **2009**, 94, 013106

[Crossref], [CAS]

72. 72.

Koenderink, A. F. On the Use of Purcell Factors for Plasmon Antennas *Opt. Lett.* **2010**, 35, 4208–4210

[Crossref], [PubMed], [CAS]

73. 73.

Jiang, G.; Pichaandi, J.; Johnson, N. J. J.; Burke, R. D.; van Veggel, F. C. J. M. An Effective Polymer Cross-Linking Strategy to Obtain Stable Dispersions of Upconverting $NaYF_4$ Nanoparticles in Buffers and Biological Growth Media for Biolabeling Applications *Langmuir* **2012**, 28, 3239– 3247

[ACS Full Text], [CAS]

74. 74.

Di
Corato, R.; Quarta, A.; Piacenza, P.; Ragusa, A.; Figuerola, A.; Buonsanti, R.; Cingolani, R.; M anna, L.;Pellegrino, T. Water Solubilization of Hydrophobic Nanocrystals by Means of Poly(Maleic Anhydride-*Alt*-1-Octadecene) *J. Mater. Chem.* **2008**, 18, 1991– 1996

[Crossref], [CAS]

75. 75.

Ariga, K.; Hill, J. P.; Ji, Q. Layer-by-Layer Assembly as a Versatile Bottom-Up Nanofabrication Technique for Exploratory Research and Realistic Application *Phys. Chem. Chem. Phys.* **2007**, 9, 2319– 2340

[Crossref], [PubMed], [CAS]

76. 76.

Shenhar, R.; Norsten, T. B.; Rotello, V. M. Polymer-Mediated Nanoparticle Assembly: Structural Control and Applications *Adv. Mater.* **2005**, 17, 657– 669

[Crossref], [CAS]

77. 77.

Park, W.; Emoto, K.; Jin, Y.; Shimizu, A.; Tamma, V. A.; Zhang, W. Controlled Self-Assembly of Gold Nanoparticles Mediated by Novel Organic Molecular Cages *Opt. Mater. Express* **2013**, 3, 205–215

[Crossref], [CAS]

78. 78.

Stutius, W.; Streifer, W. Silicon Nitride Films on Silicon for Optical Waveguides *Appl. Opt.* **1977**, 16, 3218–3222

[Crossref], [PubMed], [CAS]